Applied Catalysis B: Environmental 152–153 (2014) 129–139

Contents lists available at ScienceDirect

Applied Catalysis B: Environmental

journal homepage: www.elsevier.com/locate/apcatb

Super-high activity of Bi^{3+} doped Ag_3PO_4 and enhanced photocatalytic mechanism

Shuna Zhang [a], Shujuan Zhang [b,*,1], Limin Song [c,*,1]

[a] College of Textile Engineering, Zhejiang Industry Polytechnic College, Shaoxing, 312000, PR China
[b] College of Science, Tianjin University of Science & Technology, Tianjin 300457, PR China
[c] Tianjin Polytechnic University, College of Environment and Chemical Engineering and State Key Laboratory of Hollow-Fiber Membrane Materials and Membrane Processes, Tianjin 300387, PR China

ARTICLE INFO

Article history:
Received 27 August 2013
Received in revised form 8 January 2014
Accepted 13 January 2014
Available online 22 January 2014

Keywords:
Bi^{3+} doped Ag_3PO_4
Photodegradation
Methyl orange
OH defects
Enhanced mechanism

ABSTRACT

Bi-doped Ag_3PO_4 was synthesized by an ion exchange method, and its structure and properties were characterized systematically. Doping Bi^{3+} ions into the crystal lattice of Ag_3PO_4 changed the properties of particles, reduced the valence band position and widened the band gap of Ag_3PO_4. The doped Bi^{3+} ions have replaced P^{5+} ions of P–O tetrahedrons according to the XRD and XPS analysis. The testing of methyl orange (MO) photodegradation showed that 2 wt% Bi-doped Ag_3PO_4 had the highest activity, with the degradation rate reaching 90.7% after 6 min (1 g/L catalyst) when pure Ag_3PO_4 degraded only 27.3% of MO. Its degradation rate constant was 4.5 times that of undoped Ag_3PO_4. Particularly, 2 wt% Bi-doped Ag_3PO_4 managed to photodegrade high-concentration (40 mg/L) MO (1 g/L catalyst), with the degradation rate constant 7.3 times that of undoped Ag_3PO_4. •OH radicals were the main active species in the oxidation of MO over Bi-doped Ag_3PO_4. Doping Bi^{3+} substantially reduced OH defects on the surface of Ag_3PO_4, which significantly increased the degradation efficiency of MO over Ag_3PO_4. In addition, the density-functional theory calculation revealed that the influence of Bi dopants on the electronic structure may be an important reason for the enhanced photocatalytic performance of Ag_3PO_4.

1. Introduction

Photocatalytic technology, which is valuable in environmental pollution control, has been widely recognized and concerned [1,2]. For instance, TiO_2 photocatalytic technology can mineralize organic pollutants into non-toxic matter [3], but it suffers from high photo-generated electron–hole recombination rate, low utilization of visible light, and difficult recovery of catalyst, etc. [4]. Thereby motivated, we herein aimed to modify TiO_2 or to find new efficient and stable photocatalytic materials.

In 2010 and 2011, Ye et al. first reported Ag_3PO_4 (2.36 eV) was an efficient photocatalytic material [5,6]. By having strong binding ability, P–O bonds in the PO_4 tetrahedron of Ag_3PO_4 significantly weakened Ag–O covalent bond, prevented Ag 4d and O 2p orbits from hybridization, and deviated 4d orbit from the bottom of conduction band. Therefore, the charges at the conduction band bottom and electrons interacted mildly, which facilitated the transfer of charges to particle surface to activate redox. By first-principles calculations, Zhu et al. ascribed the superior oxidation capacity and quantum efficiency of Ag_3PO_4 to low valence band, and the much higher migration rate of electrons than that of holes owing to the π^* molecular orbits in conduction band [7]. In addition, PO_4^{3-} electrostatic induction should also be considered. Thus, the photocatalytic oxidation ability of Ag_3PO_4 is markedly increased after electrons and holes are effectively separated. Although pure Ag_3PO_4 is already photocatalytically active [8–11], fabricating stable and efficient Ag_3PO_4 photocatalytic materials with sustainable high activity remains a challenge [12].

Ion doping, including anion and cation doping [13–16], can substantially enhance the photocatalytic performance of semiconductors [17–20]. Defect energy levels in the catalyst are introduced to capture electrons and crystallization can be changed by metal cation doping. Trapping electrons can reduce the recombination probability of light-induced electrons and holes, so that numerous •OH and $\bullet O_2^-$ are generated on the semiconductor surface for activity boosting. Thus, metal cation doping not only enhances the activity of photocatalyst, but also shifts the

* Corresponding authors at: Tianjin University of Science and Technology, College of Science, Tianjin 300457, PR China. Tel.: +86 22 60600658.
E-mail addresses: zhangshujuan@tust.edu.cn (S. Zhang), songlmnk@sohu.com (L. Song).
[1] Co-first author.

0926-3373/$ – see front matter © 2014 Elsevier B.V. All rights reserved.
http://dx.doi.org/10.1016/j.apcatb.2014.01.020

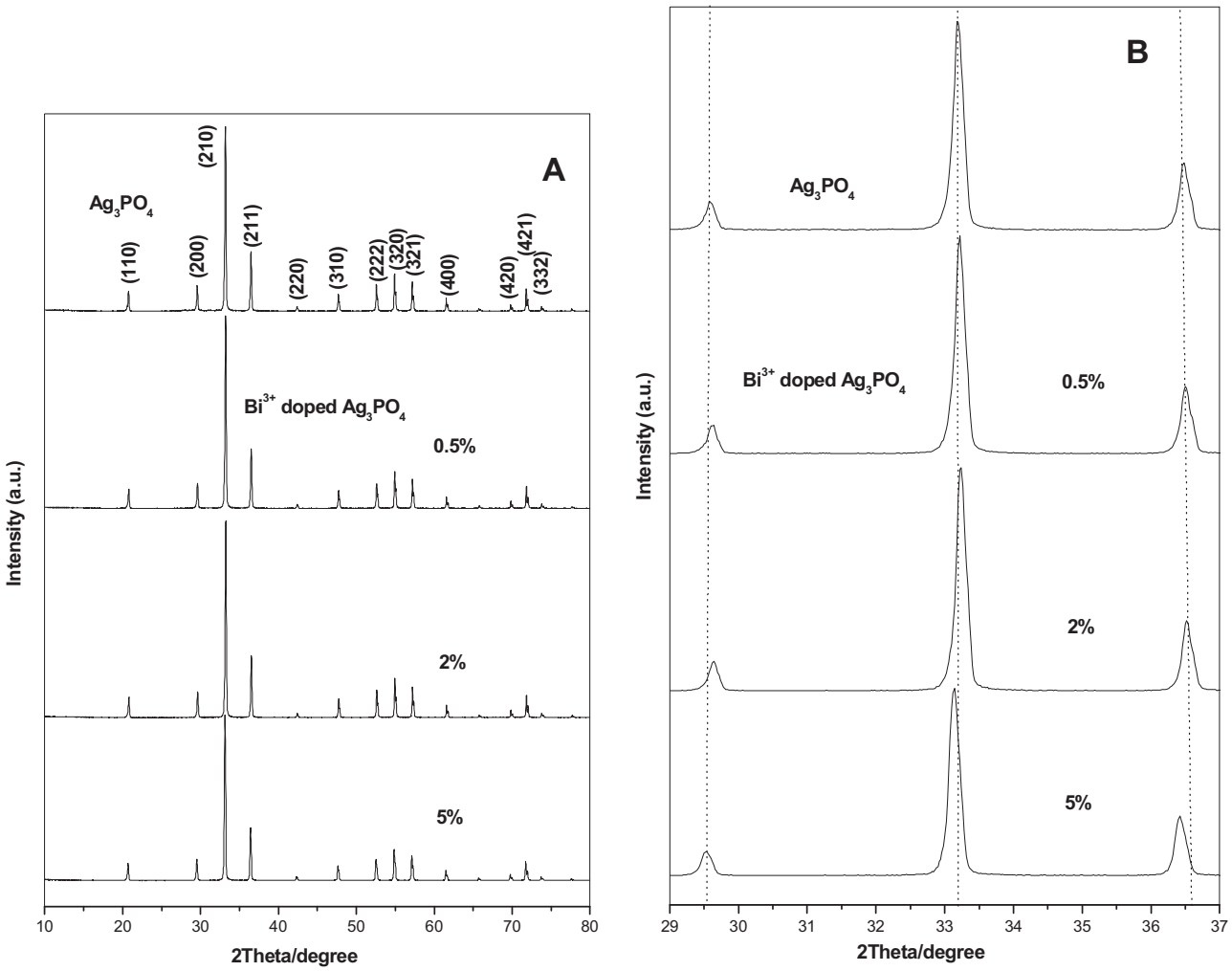

Fig. 1. X-ray diffraction patterns of undoped and Bi-doped Ag_3PO_4.

absorption edge to visible region by reducing band gap [21–23]. In this study, we prepared Bi-doped Ag_3PO_4 photocatalytic materials, and studied the photocatalytic performance and structure property of Bi-doped Ag_3PO_4. The effects of doped Bi^{3+} on the photocatalytic ability and structure of Ag_3PO_4 were also detailed.

2. Experimental

2.1. Synthesis of samples

All the chemicals were bought from Tianjin Reagent Company. All the chemicals and solvents were used without further purification. The undoped and Bi-doped Ag_3PO_4 samples were prepared by an ion-exchange method. In a typical experiment of preparing pure Ag_3PO_4, 0.002 mol $(NH_4)_3PO_4$ and 0.006 mol $AgNO_3$ were dissolved in 20 ml of distilled water, respectively. The above solutions were mixed under constant stirring for 30 min. The as-obtained precipitate was washed, and dried for 3 h at 60 °C in a vacuum oven. In order to synthesize Bi-doped Ag_3PO_4, additional $Bi(NO_3)_3$ was added to the above $AgNO_3$ solution. The other steps were same as those for the preparation of undoped Ag_3PO_4.

2.2. Characterization of samples

The powder X-ray diffraction (XRD) patterns were determined with Rigaku D/max 2500 instrument (Cu $K\alpha$, $\lambda = 1.5406$ Å, 40 kV, 40 mA). The size and morphology of samples were analyzed using a Hitachi H-7650 microscope (80 kV). UV–vis absorption spectra were recorded by HP8453 spectrophotometer ($BaSO_4$ as a reference). The binding energy (BE) was analyzed by a Perkin-Elmer PHI5300 X-ray photoelectron spectrometer (XPS). The calibration of BE is the standard peak of adventitious carbon (C_{1s}). Fourier transform infrared spectroscopy (FTIR) was determined on a Tensor37 Bruker infrared spectrometer (KBr as a reference). Total organic carbon (TOC) content of residual samples was measured by Shimadzu-Toc-Vcph. Electron spin resonance (ESR) spectra were obtained on a JES FA200 electron paramagnetic resonance spectrometer.

2.3. Activity measurement

The photodegradations of 10–40 mg/L methyl orange (MO), methylene blue (MB), rhodamine B (RhB) aqueous solutions over a series of Bi-doped Ag_3PO_4 were measured in a home-made reactor. In a typical experiment, 100 mL of 10 mg/L dye aqueous solution and 0.1 g sample were mixed and stirred for 30 min in dark to reach adsorption equilibrium. The above mixture was photoirradiated by a 300 W Xe lamp ($\lambda > 420$ nm) under continuous stirring. The residual dye solution (5 mL) was extracted every few minutes. The concentration was measured using a UV–vis spectrophotometer.

2.4. Electronic structure calculations

Calculations were performed by the density-functional theory (DFT) + U method. Geometry optimizations were carried out

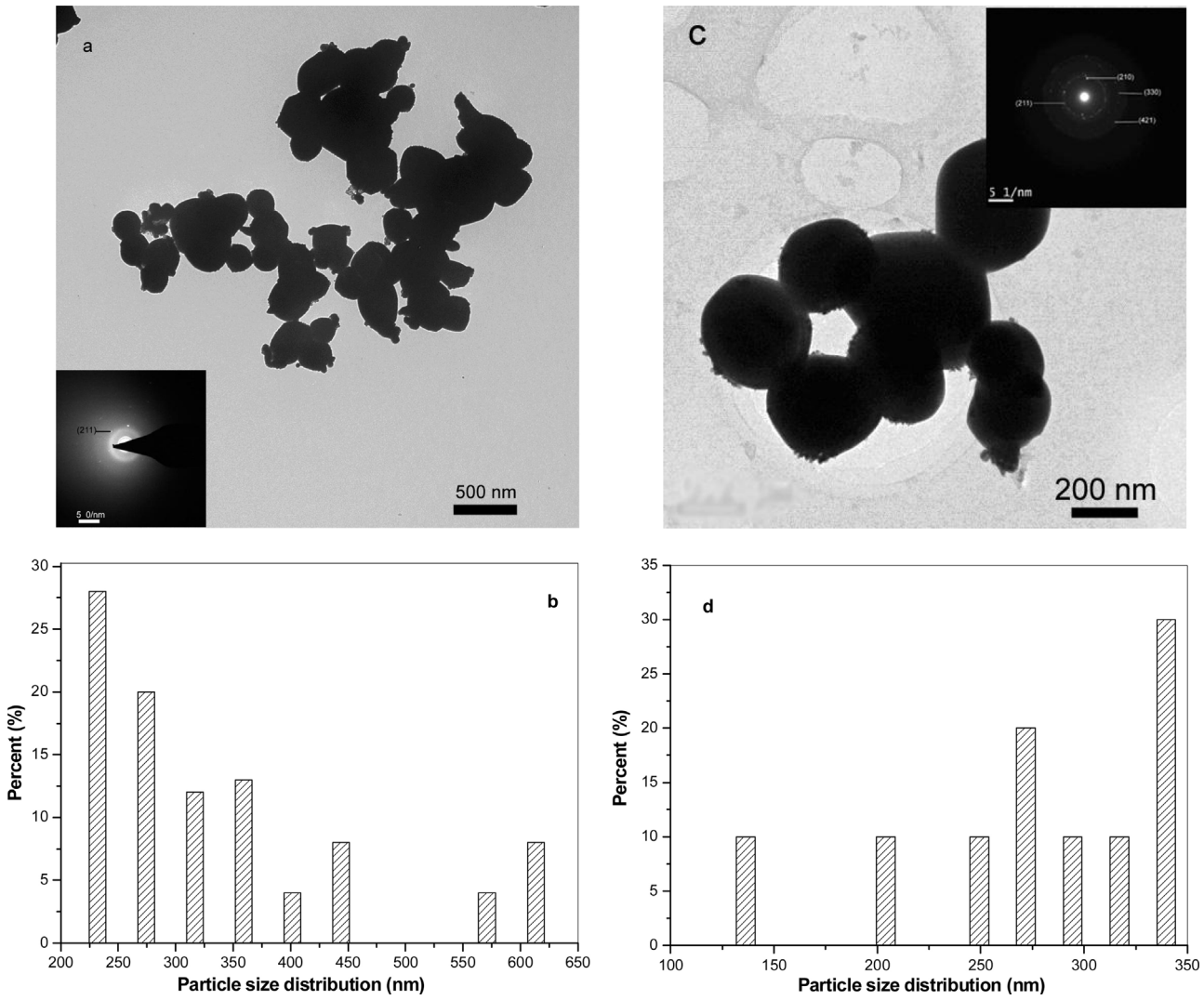

Fig. 2. TEM images of (a) Ag_3PO_4 and (c) 2 wt% Bi–Ag_3PO_4; particle mean size distribution of (b) Ag_3PO_4 and (d) 2 wt% Bi–Ag_3PO_4.

before single-point energy calculation. The exchange and correlation energy of the electrons were shown by the local-density approximation (LDA). Projector-augmented wave pseudopotentials were used as implemented in the Vienna ab initio simulations package (VASP). In the job, an energy cutoff of 400 eV and Monkhorst–Pack *k*-point sets of $2 \times 2 \times 2$ were used for a 16-atom unit cell of cubic (supercell: $2 \times 2 \times 1$) Ag_3PO_4 (space group: $P\bar{4}3n$ [218], $a = b = c = 5.89$ Å). The on-site Coulomb repulsion (Hubbard *U*) was applied for Agd, Pp, Op, and Bip states. The *U* values for Agd, Pp, Op, and Bip were set to 7.2, 7.0, 7.0, and 7.0 eV, respectively.

3. Results and discussion

3.1. Characterization of photocatalysts

XRD was performed to investigate the effects of doped Bi^{3+} on the crystal phase and structure of Ag_3PO_4. The crystal planes of undoped and doped samples (doping amounts of Bi^{3+}: 0.5, 2, and 5 wt%) have similarly positioned and shaped characteristic peaks (Fig. 1A), suggesting that the structure of Ag_3PO_4 remains unchanged after Bi^{3+} doping. These diffraction peaks can be assigned to the crystal planes of (1 1 0), (2 0 0), (2 1 0), (2 1 1), (2 2 0), (3 1 0), (2 2 2), (3 2 0), (3 2 1), (4 0 0), (4 2 0), (4 2 1) and (3 3 2) in cubic Ag_3PO_4 (JCPDS 06-0505, space group: $P\bar{4}3n$ [218], $a = b = c = 6.013$ Å). There are no peaks of impurities such as Bi_2O_3 and $BiPO_4$ in the doped Ag_3PO_4, indicating that a small amount of Bi^{3+} is evenly distributed in Ag_3PO_4. In undoped and doped Ag_3PO_4, the half-peak widths of the strongest (2 1 0) peaks decrease, which become more significant as the doping amount increases (Fig. 1B). Accordingly, we estimated the particle sizes of the samples doped with 0, 0.5, 2, and 5 wt% Bi^{3+} by the Scherer equation as 45.79, 47.94, 46.84, and 46.31 nm, respectively. We speculate that the doped Bi^{3+} ions have entered the crystal lattice of Ag_3PO_4 because all diffraction peaks of Bi-doped Ag_3PO_4 shift compared with those of pure Ag_3PO_4 (Fig. 1B). With low amount of doped Bi^{3+}, the electrostatic action of crystal planes and Bi^{3+} leads to slight lattice contraction. Therefore, all diffraction peaks of Ag_3PO_4 shift to the right. With rising amount of doped Bi^{3+} ions, those with large radius in the crystal lattice resulted in the lattice distortion of Ag_3PO_4. Hence, the lattice constants of Ag_3PO_4 increase, and the XRD peaks shift to the left. Probably, Bi^{3+} ions in Ag_3PO_4 have occupied the P^{5+} positions of in lattices. Bi^{3+} cannot exist in the interstitial site because its ionic radius (0.096 nm) is much larger than that of P^{5+} (0.035 nm).

The TEM images of representative Ag_3PO_4 and 2 wt% Bi–Ag_3PO_4 samples are shown in Fig. 2. Sphere-like pure Ag_3PO_4 particles are unevenly sized (mean size: ~328 nm) (Fig. 2a), with the particle size distribution shown in Fig. 2b. Similarly, 2 wt% Bi–Ag_3PO_4 is also sphere-like (Fig. 2c) with irregular size distribution (Fig. 2d). The

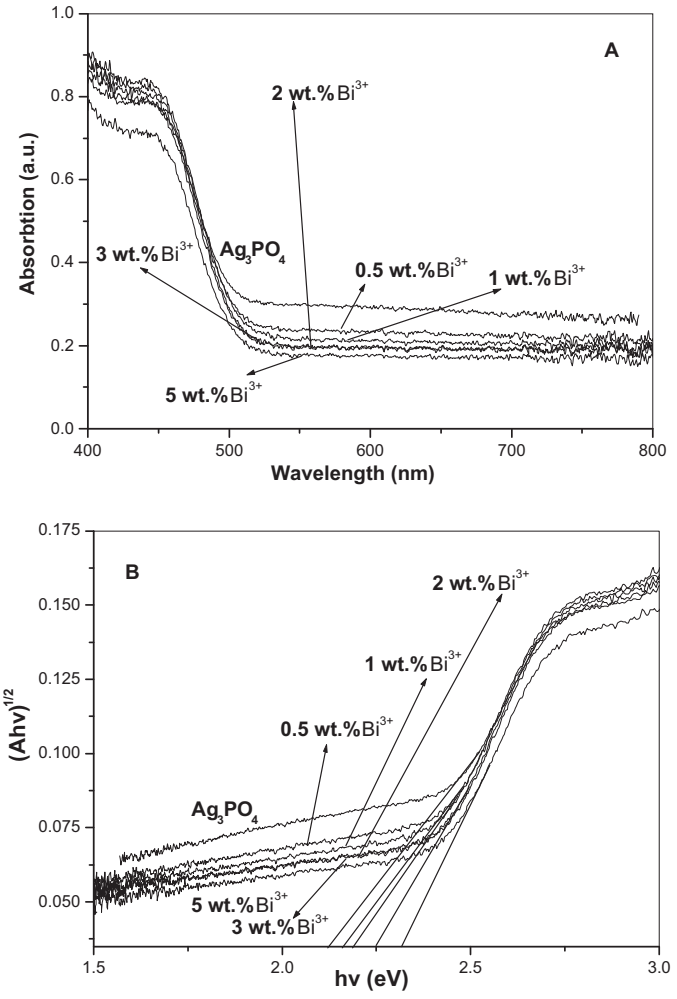

Fig. 3. UV–vis absorption spectra of the as-synthesized Ag_3PO_4 and Bi–Ag_3PO_4 samples.

mean size of 2 wt% Bi–Ag_3PO_4 is 269 nm which is smaller than that of undoped Ag_3PO_4 owing to the aggregation of crystal particles. The irregular size distributions of Ag_3PO_4 and Bi–Ag_3PO_4 particles result from the preparation method. The selected area electron diffraction (SAED) patterns of Ag_3PO_4 and 2 wt% Bi–Ag_3PO_4 exhibit latent diffuse rings (insets of Fig. 2a and c). The findings show that the as-obtained Ag_3PO_4 and Bi–Ag_3PO_4 are intrinsically polycrystalline, being in accordance with their XRD patterns. The concentric ring patterns in Fig. 2a can be attributed to the (2 1 0) plane of Ag_3PO_4, and those in Fig. 2c can be assigned to (2 1 0), (2 1 1), (3 3 0), and (4 2 1) planes.

Fig. 3A shows the UV–vis absorptions of undoped and doped Ag_3PO_4 samples that absorb visible lights at wavelengths lower than 530 nm, being consistent with a previous study [5]. All spectra of the undoped and doped Ag_3PO_4 samples possess steep edges, indicating that the visible light absorption originates from band–band transition other than the transition of impurity. Compared with those of undoped Ag_3PO_4, the absorption edges of doped Ag_3PO_4 slightly shift to short wavelength with elevating Bi^{3+} content. We estimate the band gap energies (Fig. 3B) of the samples doped with 0, 0.5, 1, 2, 3 and 5 wt% Bi^{3+} as 2.25, 2.29, 2.31, 2.35, 2.35 and 2.40 eV, respectively. The band gap values slightly increase as the doping amount of Bi^{3+} rises. Notably, Ag4d orbitals are involved in the conduction band of Ag_3PO_4, thus maintaining the position unchanged. We postulate that Bi-doping can decrease the valance band level of Ag_3PO_4 so that the band gap energy is slightly augmented with increasing Bi^{3+} content. The valance band positions of undoped and doped Ag_3PO_4 (2 wt%) were determined by XPS. According to Fig. 4A, the valance band levels of undoped and 2 wt% doped Ag_3PO_4 are 1.84 and 2.05 eV. Bi^{3+} doping can reduce the valance band level and increase the band gap value. The results accord with those of UV–vis absorption.

XPS was also conducted to investigate the chemical state and composition of sample surface. All peaks in Fig. 4 originate from Ag 3d, P 2p and Bi 4f. The 2 wt% Bi–Ag_3PO_4 sample contains Ag, P and Bi elements, which verifies Bi element has entered Ag_3PO_4. In Fig. 4B, the Ag 3d spectra of the undoped sample exhibit two sharp peaks centered around 368.8 and 374.8 eV, which can be assigned to the $3d_{5/2}$ and $3d_{3/2}$ binding energies of Ag^+ in Ag_3PO_4 [24]. The P 2p peak centered around 133.5 eV can be attributed to the binding energy of P^{5+} in Ag_3PO_4 (Fig. 4C) [25]. Obviously, the Ag 3d (369.6 and 375.5 eV) and P 2p (134.8 eV) peaks of 2 wt% Bi–Ag_3PO_4 shift to high binding energies compared with those of undoped sample. The results suggest an evident interaction between Bi, Ag and P probably due to the close proximity of them in the crystal lattice of Ag_3PO_4. Besides, Bi^{3+} can effectively decrease the electron density around Ag and P of Ag_3PO_4. In case of Bi 4f of 2 wt% Bi–Ag_3PO_4, the binding energies of $Bi_{7/2}$ and $Bi_{5/2}$ are 161.4 and 166.2 eV, respectively (Fig. 4D). According to a previous literature, Bi^{3+} in Bi_2O_3 had binding energies of 161.5 and 166.0 eV [26]. The binding energy of Bi4f peaks in 2 wt% Bi–Ag_3PO_4 changes slightly in comparison with those of Bi^{3+} in Bi_2O_3, indicating minor change of electron density around the doped Bi^{3+}. Besides, Bi^{3+} in Ag_3PO_4 substitutes for P^{5+} of P–O tetrahedrons, and ligands with surrounding O atoms, because the binding energy of Bi4f peaks in 2 wt% Bi–Ag_3PO_4 is very similar to that of Bi^{3+} forming covalent bonds with O atoms in Bi_2O_3.

Fig. 5 shows the FTIR spectra of undoped and doped Ag_3PO_4 (0–3 wt%). All FTIR spectra of the doped Ag_3PO_4 shift to high wave numbers because of the potent electron-withdrawing ability of Bi^{3+}. The characteristic vibrations at 400–1300 cm^{-1} are attributed to Ag_3PO_4 [27], and the bands at about 550 and 1010 cm^{-1} correspond to the stretching vibrations of PO_4^{3-}. The band ranging 600–700 cm^{-1} can be assigned to the stretching vibration of O–P–O. The FTIR peaks of PO_4^{3-} in 2 wt% Bi-doped Ag_3PO_4 experience significantly changed position and intensity, which further confirms that Bi^{3+} has begun to affect the crystalline phase of Ag_3PO_4. The broad absorptions at around 3200–3600 and 1680 cm^{-1} represent intrinsic OH stretching and bending vibrations [28], and that at about 1377 cm^{-1} is assigned to the OH vibrations of H_2O molecules adsorbed on the sample surface [29]. OH defect concentration can be distinguished from the infrared vibration spectrum [30–32]. OH defect concentration is proportional to the FTIR peak area [33]. OH stretching vibrations at 3200–3600 cm^{-1} plummet after Bi-doping (Fig. 5) that significantly decreases OH defect concentration on the Ag_3PO_4 surface.

The band structure and density of states (DOS) of pure and Bi^{3+} doped Ag_3PO_4 were calculated by the LDA + U method. For the undoped Ag_3PO_4, the band gap value obtained by LDA was 2.488 eV (Fig. 6A), which was higher than the experimental value (2.25 eV) due to the limitation of DFT. Fig. 6B shows the atomic DOSs of Ag_3PO_4. The tops of the valence bands comprised hybridized Ag 4d and O 2p orbitals. The bottoms of the conduction bands were mainly derived from hybridized Ag 5s, Ag 5p and P 3p orbitals. The result was slightly different from those reported by Ye et al. previously [5]. Fig. 7 exhibits the structure and atomic DOSs of Bi–Ag_3PO_4 calculated by LDA. There were three isolated doping states of Bi (Fig. 7A). They were mainly derived from Bi 6s to Bi 6p orbitals (Fig. 7B). There was also a small amount of contributions of O 2s, O 2p, Ag 5s, and Ag 5p in these doping states (Fig. 8), indicating the interaction between doped Bi, O and Ag atoms. In comparison with the band structure and DOSs of pure Ag_3PO_4 (Fig. 6), the Bi dopants did not significantly affect the component and location of the band structure (Fig. 7).

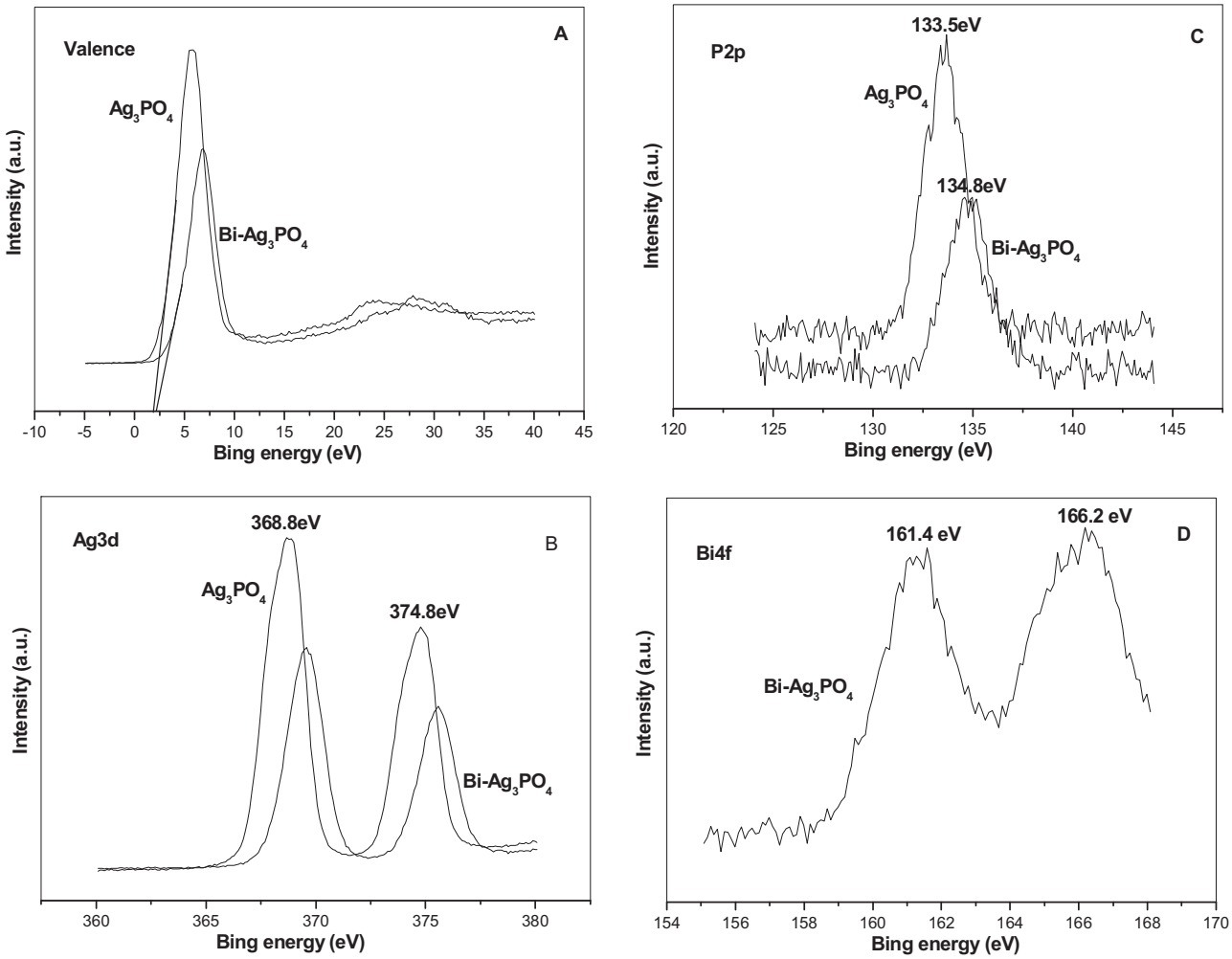

Fig. 4. XPS spectra of the as-synthesized Ag_3PO_4 and 2 wt% Bi–Ag_3PO_4 samples. (A) valence, (B) Ag_{3d}, (C) P_{2P}, (D) Bi_{4f}.

The main effect of the Bi dopants in Ag_3PO_4 was to reduce the band gap (1.954 eV for Bi–Ag_3PO_4) and to introduce the doping bands in the primary band structure. The results may be responsible for the enhanced photocatalytic performance of Ag_3PO_4.

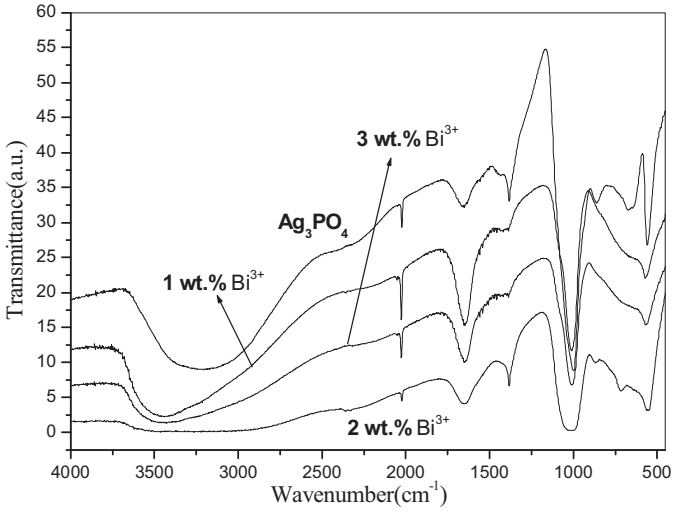

Fig. 5. IR spectra of the as-synthesized Ag_3PO_4 and Bi–Ag_3PO_4 samples.

3.2. Photocatalytic activity of photocatalysts

It is well known that doping concentration affects the activity of photodegradation. To determine the optimum doping amount of Bi^{3+}, Ag_3PO_4 samples doped with 0.0 to 5.0 wt% Bi^{3+} were used to photodegrade MO for 14 min (Fig. 9A). All the catalysts were stirred in dark for 30 min to reach adsorption equilibrium before photocatalytic reaction. The adsorption amounts of all the doped samples are higher than that of undoped Ag_3PO_4 (Fig. 9A). MO molecules are negatively charged in aqueous solution, and Bi^{3+} ions are positively charged in doped Ag_3PO_4. Ergo, internal attraction between the positive and negative charges of Bi^{3+} and MO augments the adsorption capacity on the surface of Ag_3PO_4. Nevertheless, the adsorption capacity of Bi-doped Ag_3PO_4 is lower than 10%, i.e. the photocatalytic activity is not significantly influenced. All Bi-doped Ag_3PO_4 samples exhibit higher photocatalytic activities than pure Ag_3PO_4 (Fig. 9A), and the photocatalytic activities of Bi-doped Ag_3PO_4 fluctuate with elevating Bi^{3+} amount. Being most photocatalytically active, 2 wt% Bi-doped Ag_3PO_4 degrades 90.7% of MO within 6 min. In contrast, only 27.3% of MO molecules are degraded after 6 min in the presence of pure Ag_3PO_4. Moreover, the photodegradation rates of 0.5, 1, 3, and 5 wt% Bi-doped samples are 39.8, 40.33, 49.52, and 64.35% after 6 min. In other words, the optimum doping amount of Bi^{3+} is 2 wt%. According to Fig. 6A, the reaction rate constants (k) are 0.0828, 0.0859, 0.1574, 0.3764, 0.1321 and 0.1692 min^{-1} for 0, 0.5, 1, 2, 3 and 5 wt% Bi-doped samples, respectively (Fig. 9B). The rate constant of 2 wt% Bi-doped Ag_3PO_4 is 4.5 times that of

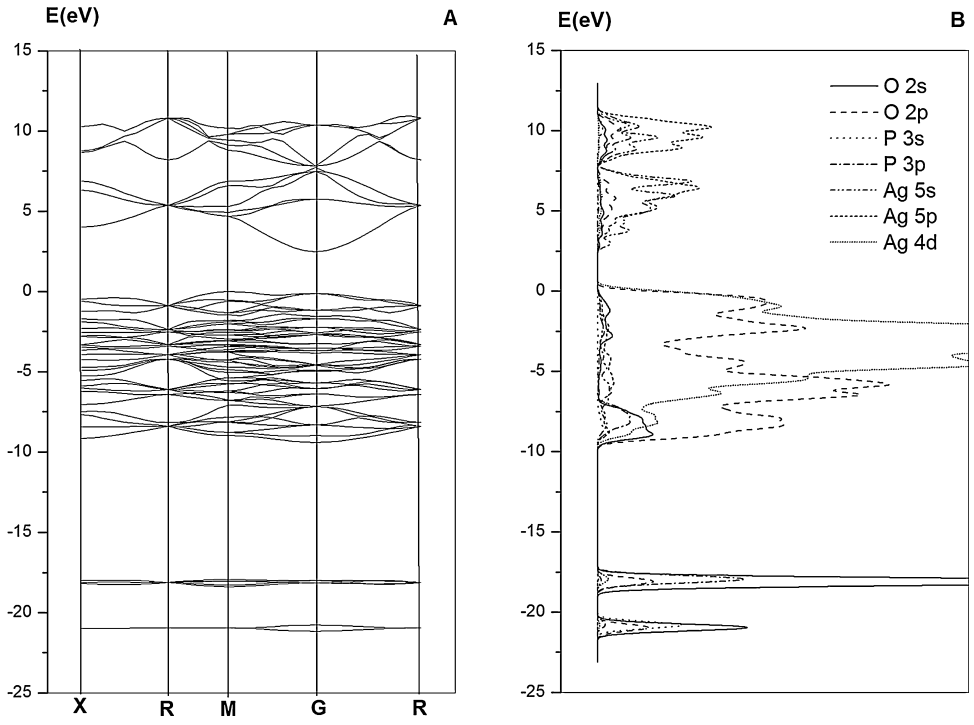

Fig. 6. (A) Band structure and (b) atomic DOSs for Ag_3PO_4.

Ag_3PO_4. Apparently, Bi^{3+} doping can remarkably enhance the photocatalytic performance. Fig. 10 presents the influences of MO concentration on the photodegradation rate in the presence of pure and 2 wt% Bi-doped Ag_3PO_4. The photodegradation rates of Ag_3PO_4 plummet with rising MO concentration from 10 to 40 mg/L (Fig. 10A). The photocatalytic activities for 30 and 40 mg/L MO are 57.8 and 44% after 60 min. Compared to those of pure Ag_3PO_4, the photocatalytic activities of 2 wt% Bi-doped Ag_3PO_4 slightly change (Fig. 10B). The photocatalytic activities for 30 and 40 mg/L MO reach around 80% after about 22 min. The reaction rate constants over pure Ag_3PO_4 are 0.0828, 0.0480, 0.0098 and 0.0098 min^{-1} for 10–40 mg/L MO, respectively (Fig. 10C), and those over 2 wt% Bi-doped Ag_3PO_4 are 0.3764, 0.1480, 0.0715 and 0.0715 min^{-1}, respectively (Fig. 10D). Clearly, the rate constants of 2 wt% Bi-doped Ag_3PO_4 are 4.5, 3.0, 7.3, and 7.3 times those of Ag_3PO_4 for 10–40 mg/L MO. The above results indicate that Bi-doped Ag_3PO_4 remains active against high-concentration MO solution. The enhanced photocatalytic activity for MB (20 mg/L)

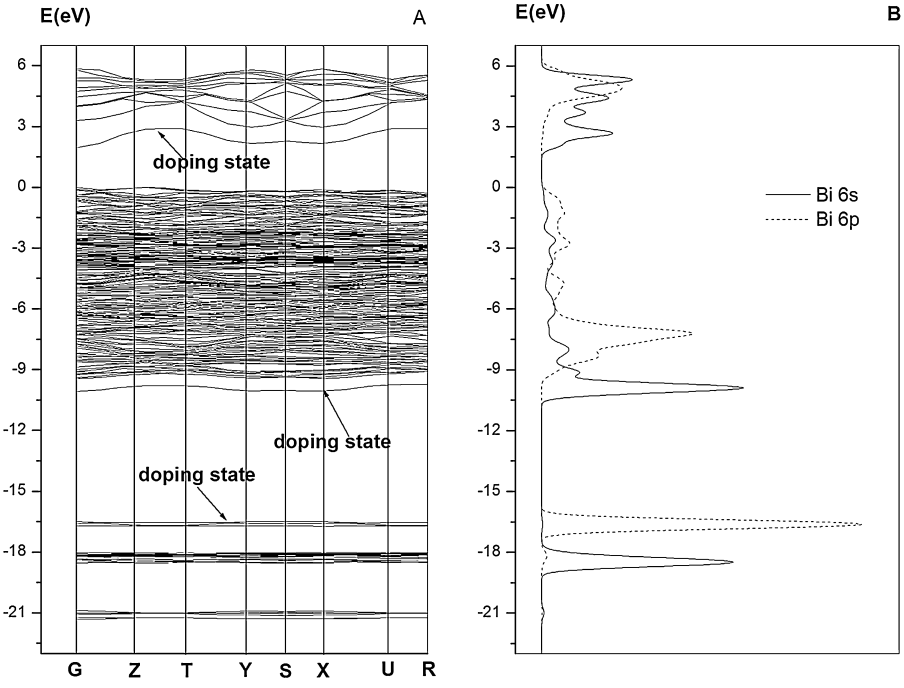

Fig. 7. (A) Band structure and (b) Bi atomic DOSs for Bi-Ag_3PO_4.

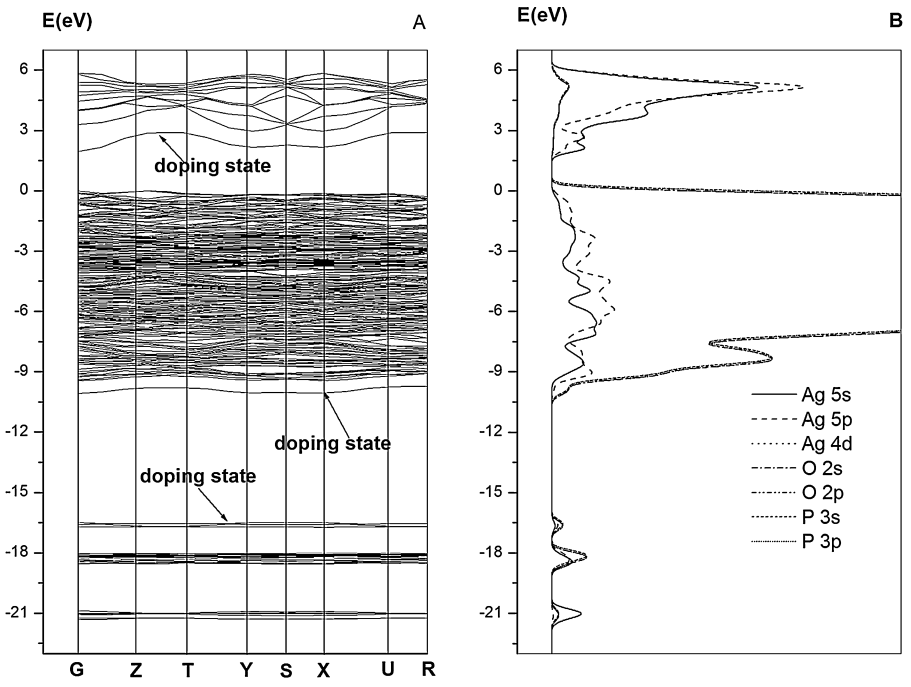

Fig. 8. (A) Band structure and (b) Ag, O, P atomic DOSs for Bi-Ag_3PO_4.

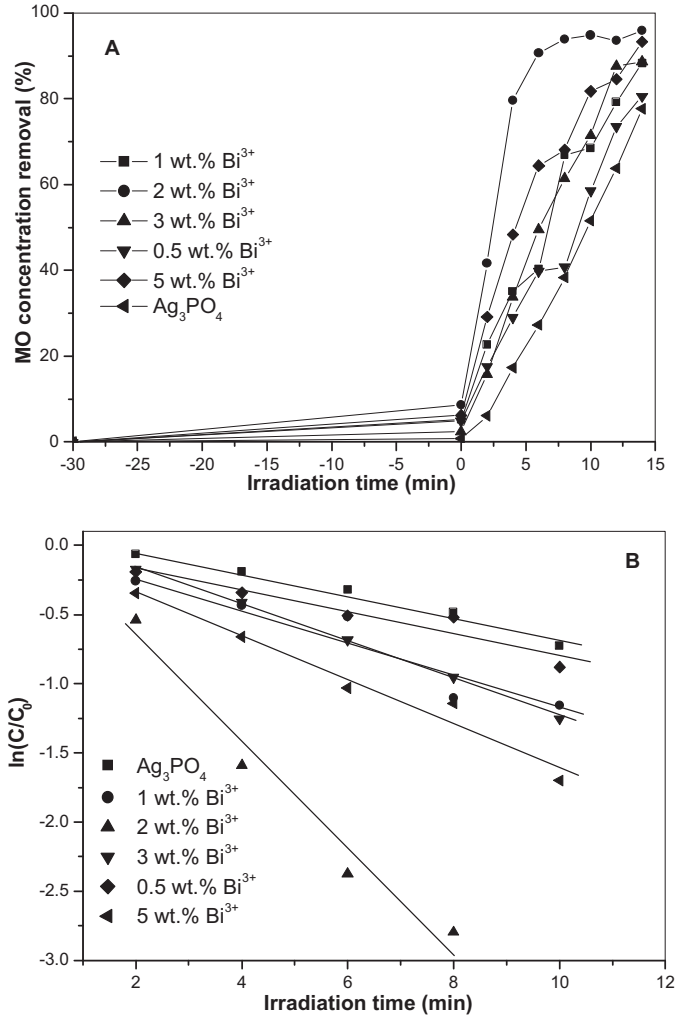

Fig. 9. (A) The dependence of photocatalytic activity on the doped Bi^{3+} content. (B) The relationship between $\ln(C/C_0)$ and irradiation time.

and RhB (10 mg/L) solution over 2 wt% Bi-doped Ag_3PO_4 can also be observed in Fig. 11. It is found that 2 wt% Bi-doped Ag_3PO_4 degrades 94.66% of MB and 93.3% of RhB within 10 min in Fig. 11A and 11 C, while only 81.4% of MB and 82.3% of RhB can be degraded in 10 min in the presence of Ag_3PO_4. The reaction rate constants on 2 wt% Bi-doped Ag_3PO_4 are 0.2784 and 0.2207 min^{-1} for 20 mg/L MB and 10 mg/L RhB, respectively, and those over Ag_3PO_4 are 0.1774 and 0.1468 min^{-1}, respectively (Fig. 11B and D). Compared with the above result, the rate constants of 2 wt% Bi-doped Ag_3PO_4 are 1.6 and 1.5 times those of Ag_3PO_4 for 20 mg/L MB and 10 mg/L RhB, respectively. To explore the reusability of Bi-doped Ag_3PO_4, photodegradation experiments over 2 wt% Bi-doped Ag_3PO_4 were repeated (Fig. 12), during which the solution of MO was filtered, and the residual was washed and dried to be evaluated for next degradation cycle under the same conditions. Particularly, 2 wt% Bi-doped Ag_3PO_4 remained highly photocatalytically active (over 92%) after 10 cycles.

The 2 wt% Bi-doped Ag_3PO_4 after the first run was characterized by UV–vis absorption spectroscopy and XRD (Fig. 13). The UV–vis absorption spectrum of the doped sample is similar to that of the fresh sample (Fig. 13A). However, the maximum absorption of the sample slightly shifted to long wavelength, which can be attributed to the additional Ag_2O particles on the surface of the used 2 wt% Bi-doped Ag_3PO_4 (Fig. 13B). The peak at 32.5° corresponds to the (1 1 1) plane of Ag_2O. However, the XRD peaks of Ag were absent. In other words, there were only Ag_2O particles on the surface of the used 2 wt% Bi-doped Ag_3PO_4. It is well known that Ag^+ compounds are not stable under visible light irradiations because Ag^+ can be reduced by photogenerated electrons to Ag nanoparticles. In this study, the as-formed Ag particles reacted further with O_2 in the dye solution to produce Ag_2O [34]. Ag_2O, as a stable material, was responsible for the stable photocatalytic performance of 2 wt% Bi-doped Ag_3PO_4 after many runs after being deposited.

3.3. Improved photocatalytic mechanism

UV–vis absorption spectra of the photodegradation of 40 mg/L MO solution over 2 wt% Bi-doped Ag_3PO_4 are given in Fig. 14A. The

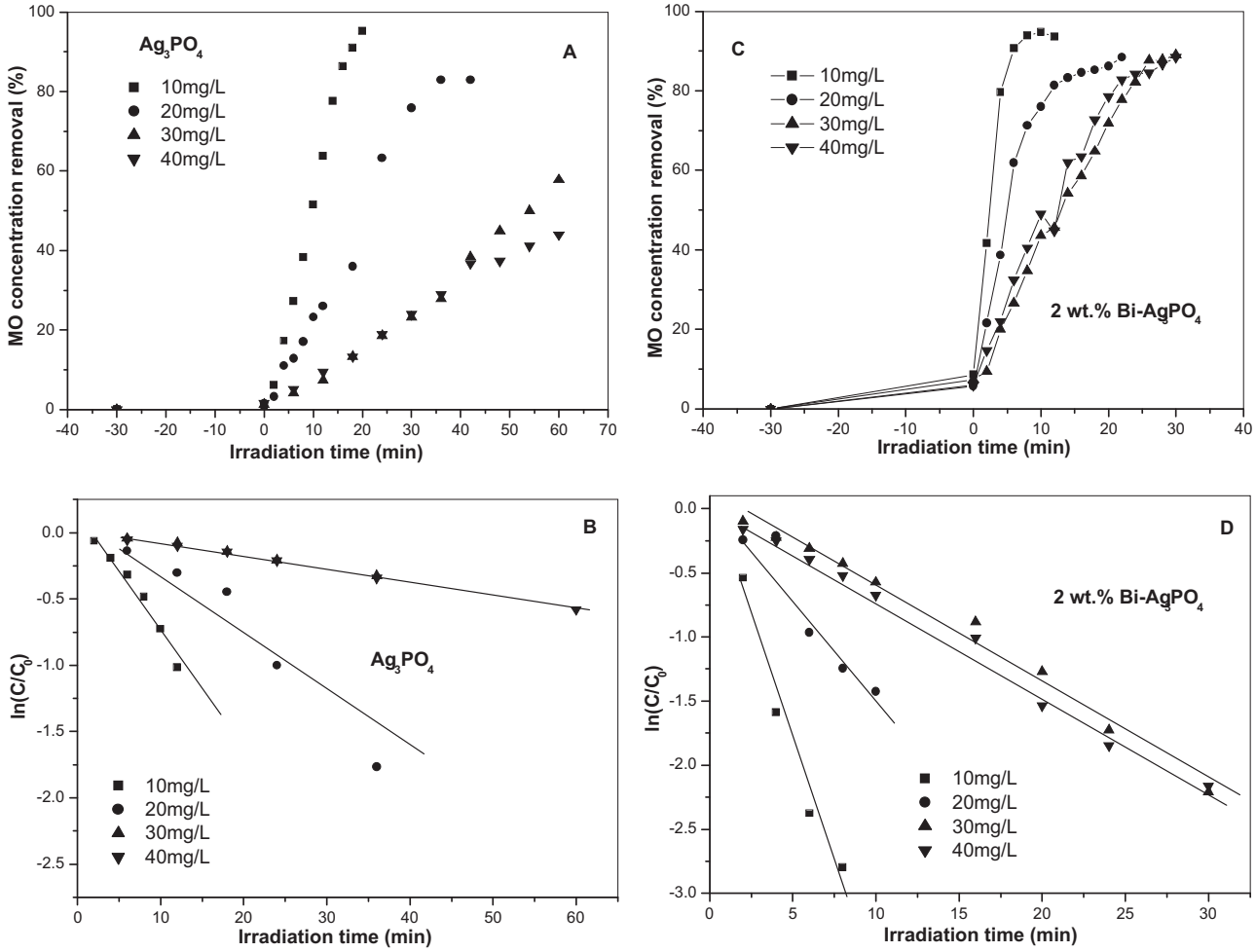

Fig. 10. The dependence of photocatalytic activity on the original concentration over (A) Ag_3PO_4 and (C) Bi–Ag_3PO_4. The relationship between $\ln(C/C_0)$ and irradiation time of (B) Ag_3PO_4 and (D) Bi–Ag_3PO_4.

absorption peaks at 292 and 465 nm can be attributed to the characteristic groups of MO. The weak peak at 292 nm corresponds to the absorption of benzene ring caused by $\pi \rightarrow \pi^*$ electronic transitions, and the intense absorption peak at 465 nm is induced by the $n \rightarrow \pi^*$ electronic transitions from the hydrazone structure of MO. There are no other absorption peaks from 200 to 800 nm. However, the intensities of two characteristic MO peaks gradually decrease with elapsed time, suggesting that MO molecules have been degraded under experimental conditions. To clarify the final products after decomposition, the total organic carbon (TOC) values of residual MO after the photodegradation of 10 mg/L MO solution over 2 wt% Bi-doped Ag_3PO_4 were measured (Fig. 14B), which are obviously reduced with prolonged reaction, i.e. part of MO molecules have been decomposed into CO_2 and H_2O. However, the decreased TOC values are not consistent with the photodegradation rates of MO solution (Fig. 9A). The results reveal that partial intermediate products have formed other than decomposed into CO_2 and H_2O.

Generally, organic dyes are photooxidized mainly by active species such as •OH, $\bullet O_2$-, and photogenerated holes. •OH instead of $\bullet O_2$- radicals predominate in the photocatalysis of liquid phase reaction because $\bullet O_2$- radicals are bound to be converted into •OH. Mechanism regarding the direct oxidation of organics by photogenerated holes mainly applies to organic matter without C–H bonds. According to reference [13], the •OH radicals can be confirmed by the ESR spin trap with the DMPO technique. Therefore, the •OH radicals in the photooxidation of MO over 2 wt% Bi-Ag_3PO_4 were monitored by ESR spectroscopy to confirm the oxidation mechanism (Fig. 15). It is very clear that the typical signals of DMPO–OH under visible light irradiation ($\lambda > 420$ nm) can be detected in the 2 wt% Bi–Ag_3PO_4 system (Fig. 15a), while a small amount of characteristic signals for DMPO–OH in dark is detected in the 2 wt% Bi–Ag_3PO_4 system (Fig. 15b). The above result indicates that •OH radicals are the main active species that oxidize MO molecules over Bi-doped Ag_3PO_4. We postulate the possible reaction mechanism as follows:

$$\text{Bi–Ag}_3\text{PO}_4 + h\nu \rightarrow \text{h}^+ + \text{e}^-$$

$$\text{OH}^- + \text{h}^+ \rightarrow \bullet\text{OH}$$

$$\text{O}_2 + \text{e}^- \rightarrow \bullet\text{O}_2- \rightarrow \bullet\text{OOH} \rightarrow \text{H}_2\text{O}_2 \rightarrow \bullet\text{OH}$$

$$\text{OH} + \text{MO} \rightarrow \text{products}$$

The improved activities of the doped samples stem from the nature of Ag_3PO_4. According to the classical theory of photocatalytic reaction, photocatalysis is favored in case of high specific surface area, small particle size, low valence band position and thorough electron–hole separation. For Bi-doped Ag_3PO_4, the particle size (micro-level) and specific surface area (powders without

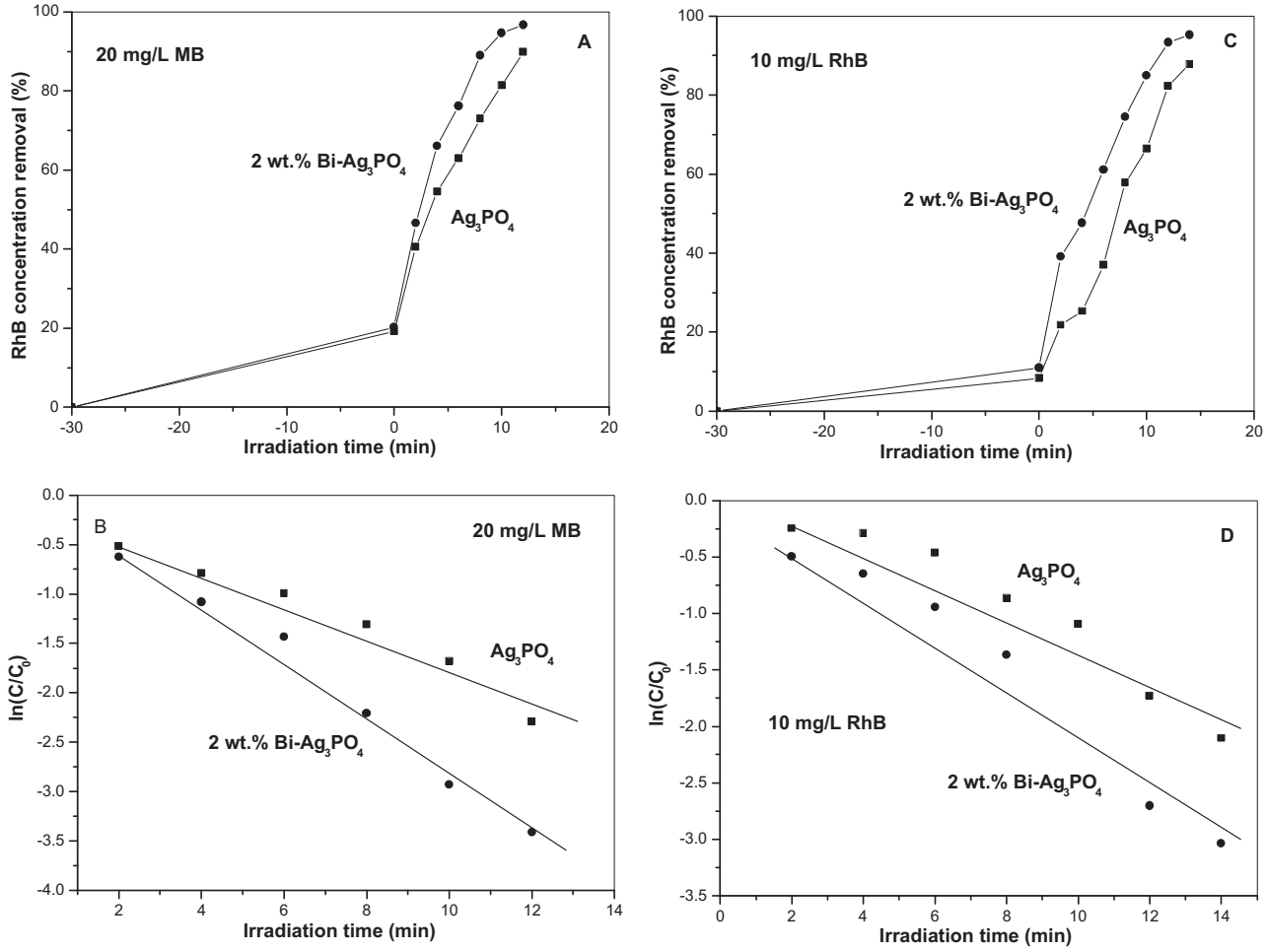

Fig. 11. The photodegradation activity (A) MB and (C) RhB over Ag_3PO_4 and 2 wt% Bi-Ag_3PO_4. The relationship between $\ln(C/C_0)$ and irradiation time of (B) MB and (D) RhB.

pores) of Ag_3PO_4 are not significantly varied after Bi doping, and the band gap increases slightly with rising Bi amount. Low valence band position boosts the photocatalytic activity of Ag_3PO_4 by facilitating the mobility of photogenerated holes. Nevertheless, the results are inconsistent with the activity of Bi-doped Ag_3PO_4. The photocatalytic activities of Bi-doped Ag_3PO_4 increase irregularly with increasing dopants (Fig. 9A), of which 2 wt% Bi-doped Ag_3PO_4 functions optimally. Therefore, the above factors do not considerably contribute to the enhanced photocatalytic activity. Based on previous references and above analyses [12], we hold that OH defects form on the surface of Ag_3PO_4 because of low energy (0.5 eV). Oxygen and H^+ ions in lattice form OH^- in solution, resulting in OH defects by replacing the oxygen of P–O tetrahedrons. Meanwhile, excess positive charge can be supplemented by Ag^+-produced vacancies. High-concentration OH defects can prevent electron transitions and accelerate electronic recombination by destroying Ag–O bonds in Ag_3PO_4. Besides, OH defects raise valence band positions and lower conduction ones by narrowing band gap, thus suppressing the transfer of electron and hole and yielding •OH and $\bullet O_2^-$ radicals on the interface of Ag_3PO_4. Finally, OH defects affect the photocatalytic ability of Ag_3PO_4. Doped Bi^{3+} ions are positively charged, and OH defects also produce excess positive charges. Doping Bi^{3+} in Ag_3PO_4 inhibits the formation of excess OH defects because of repulsion. As shown in Fig. 5, OH defects on the surface of Bi-doped Ag_3PO_4 are significantly less than those of pure Ag_3PO_4. Therefore, all Bi-doped Ag_3PO_4 samples are more active than undoped Ag_3PO_4. 2 wt% Bi-doped Ag_3PO_4, which has minimum OH defects, is most active (Fig. 9A). Hence, reduced OH defects by Bi^{3+} doping primarily account for the boosted photocatalytic ability of Ag_3PO_4 besides the influence Bi dopants on the electronic structure.

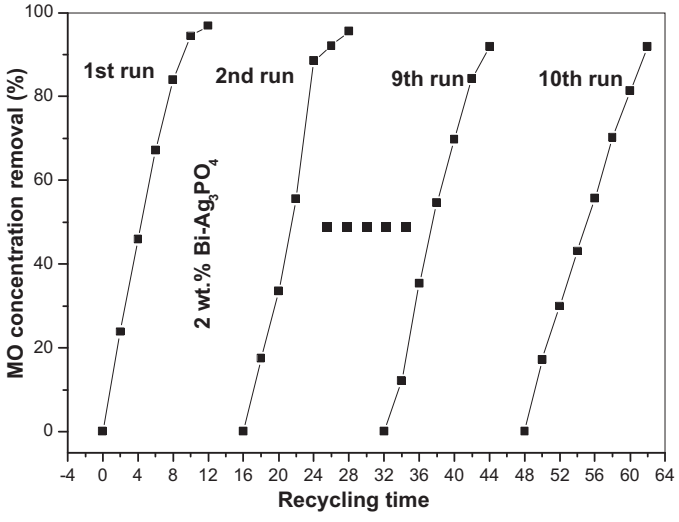

Fig. 12. Recycling tests of degradation of 10 mg/L MO over 2 wt% Bi–Ag_3PO_4. The concentration of catalysts is 1.0 g/L.

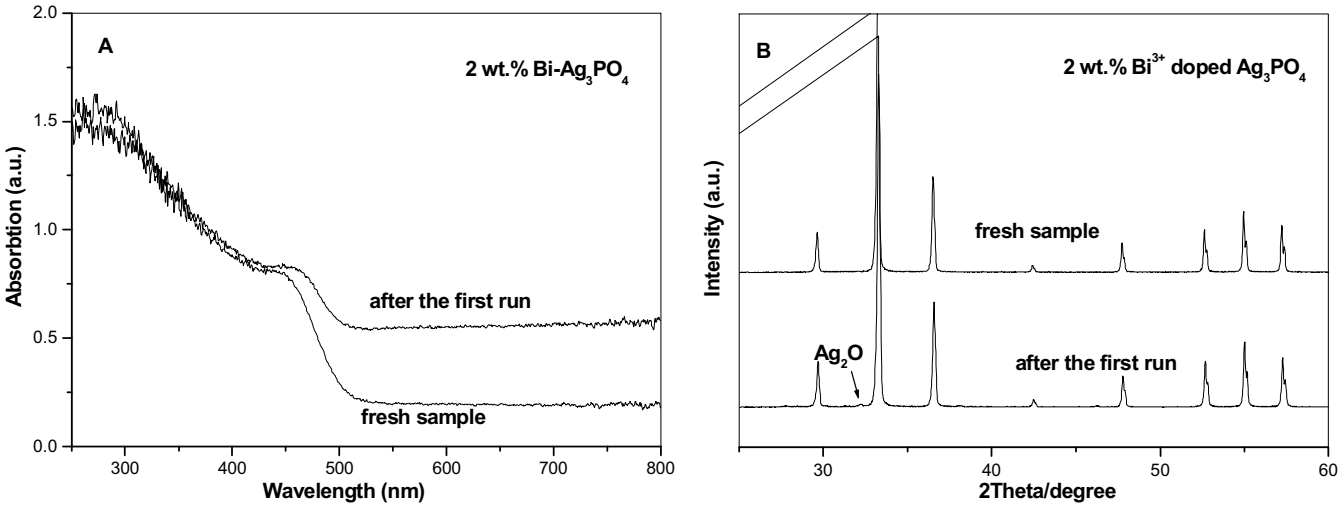

Fig. 13. The absorption spectra (A) and XRD (B) after the first run.

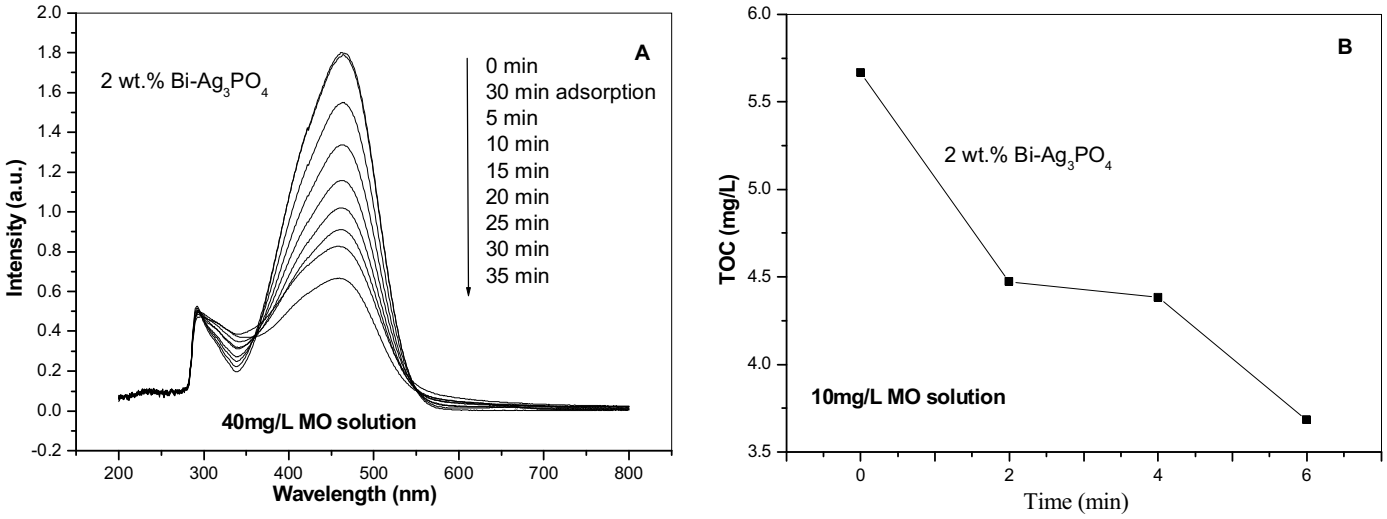

Fig. 14. (A) The UV–vis absorption spectra of solution in the process of the photocatalytic degradation of 40 mg/L MO on 2 wt% Bi–Ag_3PO_4. The concentration of catalysts is 1.0 g/L. (B) TOC evolution versus irradiation time in the photocatalytic reaction.

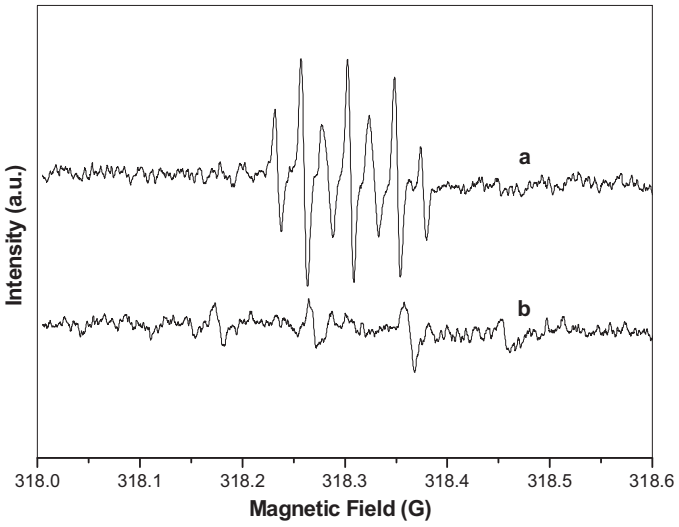

Fig. 15. DMPO spin-trapping ESR spectra for DMPO–OH in the presence of 2 wt% Bi–Ag_3PO_4 (a) under visible light irradiation ($\lambda > 420$ nm), (b) in dark.

4. Conclusion

In short, a series of Bi-doped Ag_3PO_4 photocatalytic materials were prepared. The doped Bi^{3+} ions dramatically affected the structure and performance of Ag_3PO_4 particles, and rendered Ag_3PO_4 more photocatalytically active. We ascribe the results to the reduction of OH defects by Bi^{3+} doping and the influence of Bi dopants on the electronic structure in Ag_3PO_4.

References

[1] A.J. Bard, J. Photochem. 10 (1979) 59–75.
[2] C.C. Chen, J.C. Zhao, W.H. Ma, Chem. Soc. Rev. 39 (2010) 4206–4219.
[3] S.U.M. Khan, M. Al-Shahry, W.B. Ingler, Science 297 (2002) 2243–2245.
[4] U.G. Akpan, B.H. Hameed, J. Hazard. Mater. 170 (2009) 520–529.
[5] Z.G. Yi, J.H. Ye, N. Kikugawa, T. Kako, S.X. Ouyang, H.S. Williams, H. Yang, J.Y. Cao, W.J. Luo, Z.S. Li, Y. Liu, R.L. Withers, Nat. Mater. 9 (2010) 559–564.
[6] Y.P. Bi, S.X. Ouyang, N. Umezawa, J.Y. Cao, J.H. Ye, J. Am. Chem. Soc. 133 (2011) 6490–6492.
[7] X.G. Ma, B. Lu, D. Li, R. Shi, C.S. Pan, Y.F. Zhu, J. Phys. Chem. C 115 (2011) 4680–4687.
[8] H. Wang, Y.S. Bai, J.T. Yang, X.F. Lang, J.H. Li, L. Guo, Chem.—Eur. J. 18 (2012) 5524–5529.
[9] H.C. Zhang, H. Huang, H. Ming, H.T. Li, L.L. Zhang, Y. Liu, Z.H. Kang, J. Mater. Chem. 22 (2012) 10501–10506.

[10] C.T. Dinh, T.D. Nguyen, F. Kleitzb, T.O. Do, Chem. Commun. 47 (2011) 7797–7799.
[11] Y.P. Bi, H.Y. Hu, S.X. Ouyang, Z.B. Jiao, G.X. Lu, J.H. Ye, J. Mater. Chem. 22 (2012) 14847–14850.
[12] H. Tong, S.X. Ouyang, Y.P. Bi, N. Umezawa, M. Oshikiri, J.H. Ye, Adv. Mater. 24 (2012) 229–251.
[13] S.W. Hu, J. Zhu, L. Wu, X.X. Wang, P. Liu, Y.F. Zhang, Z.H. Li, J. Phys. Chem. C 115 (2011) 460–467.
[14] S.J. Liang, S.Y. Zhu, J. Zhu, Y. Chen, Y.F. Zhang, L. Wu, Phys. Chem. Chem. Phys. 14 (2012) 1212–1222.
[15] Z.H. Li, H. Dong, Y.F. Zhang, T.T. Dong, X.X. Wang, J.Q. Li, X.Z. Fu, J. Phys. Chem. C 112 (2008) 16046–16051.
[16] Z.H. Li, T.T. Dong, Y.F. Zhang, L. Wu, J.Q. Li, X.X. Wang, X.Z. Fu, J. Phys. Chem. C 111 (2007) 4727–4733.
[17] R. Asahi, T. Morikawa, T. Ohwaki, K. Aoki, Y. Taga, Science 293 (2001) 269–271.
[18] Q. Zhang, D.Q. Lima, I. Lee, F. Zaera, M.F. Chi, Y.D. Yin, Angew. Chem. Int. Ed. 50 (2011) 7088–7092.
[19] T. Yang, H. Wang, X.M. Ou, C.S. Lee, X.H. Zhang, Adv. Mater. 24 (2012) 6199–6203.
[20] K. Hashimoto, H. Irie, A. Fujishima, J. Appl. Phys. 44 (2005) 8269–8285.
[21] I. Justicia, P. Ordejon, G. Canto, Adv. Mater. 14 (2002) 1399–1402.
[22] G. Liu, L.Z. Wang, H.G. Yang, H.M. Cheng, G.Q. Lu, J. Mater. Chem. 20 (2010) 831–843.
[23] L.P. Li, J.J. Liu, Y.G. Su, G.S. Li, X.B. Chen, X.Q. Qiu, T.J. Yan, Nanotechnology 20 (2009) 155706–155715.
[24] H. Zhang, G. Wang, D. Chen, X.J. Lv, J.H. Li, Chem. Mater. 20 (2008) 6543.
[25] R.Y. Zheng, L. Lin, J.L. Xie, Y.Z. Zhu, Y.C. Xie, J. Phys. Chem. C 112 (2008) 15502–15509.
[26] F.M. Ismail, Z.M. Hanafi, Z. Phys. Chem. (Leipzig) 267 (1986) 667.
[27] K. Vivekanandan, S. Selvasekarapandian, P. Kolandaivel, Mater. Chem. Phys. 39 (1995) 284–289.
[28] G. Huang, S. Zhang, T. Xu, Y. Zhu, Environ. Sci. Technol. 42 (2008) 8516–8521.
[29] H. Abbas, S.A. Nasser, J. Power Sources 58 (1996) 15–21.
[30] P.W. Peacock, J. Robertson, Appl. Phys. Lett. 54 (2003) 2025–2027.
[31] M. Rail, D. Zhou, E.G. Kisvarsanyi, N.S. Sullivan, Phys. Rev. B: Condens. Matter 45 (1992) 2800–2807.
[32] J. Robertson, P.W. Peacock, Thin Solid Films 445 (2003) 155–160.
[33] P. Beneventit, R. Capelletti, L. Kovács, Á. Péter, A.M.L. Manotti, F. Ugozzoli, J. Phys. Conf. Ser. 6 (1994) 6329–6344.
[34] W.J. Liu, X.B. Liu, Y.H. Fu, Q.Q. You, R.K. Huang, P. Liu, Z.H. Li, Appl. Catal., B 123–124 (2012) 78–83.